Analysis of Path Loss from a Transmitter in an Aircraft Cabin to an Exterior Fuselage-Mounted Antenna

Kathy Weiquan Wang-Hurst

Thesis submitted to the Faculty of the
Virginia Polytechnic Institute and State University
in partial fulfillment of the requirements for the degree of

Master of Science
in
Electrical Engineering

Steven W. Ellingson, Chair
Wayne Scales
Brent Ledvina

December 4, 2007
Blacksburg, Virginia

Keywords: Indoor Propagation, Aircraft Antennas, Electromagnetic Compatibility

Analysis of Path Loss from a Transmitter in an Aircraft Cabin to an Exterior Fuselage-Mounted Antenna

Kathy Weiquan Wang-Hurst

ABSTRACT

It is important to investigate the threat posed to commercial aircraft by on board electronic transmitters in the passenger cabin and the cargo holds of large transport aircraft. These transmitters may be in the form of unintentional use of portable electronic devices or even intentional radio frequency (RF) threat sources from terrorists. Thus, it is of interest to determine the "interference path loss" (IPL) from a transmitting device inside the cabin of such aircraft to the antenna terminals of a potential victim system of the aircraft. Past studies have concentrated on measurements. These efforts to measure IPL directly have demonstrated that accurate and repeatible measurements are difficult to obtain. Very little modeling work has been done successfully to understand the IPL on aircraft. In this thesis, we propose a 3-step methodology to quantify the interference path loss (IPL). We then apply this methodology to a broad class of aircraft and show results. To validate our results, we compare our findings to known measurements and discuss possible sources of errors. Finally we suggest areas of improvement to our analysis and propose future work.

Acknowledgments

Parts of this work were supported under Contract No. 29531 from the Aerospace Vehicle Systems Institute (AVSI) to the Virginia Polytechnic Institute and State University.

I'd like to take this opportunity to thank my advisor, Dr. Ellingson, for his infinite patience and tireless support during the entire process of my thesis. His brilliant mind and unlimited energy made everything possible.

Contents

List of Figures

List of Tables

Chapter 1

Introduction

Modern aircraft use a complex suite of electronic systems for communication and navigation [1]. Flight safety depends on the unimpeded operation of these systems. There have been concerns on the threat posed to communication and navigation systems of commercial aircraft by on board transmitters in the passenger cabin and the cargo area. These transmitters may be in the form of unintentional use of portable electronic devices such as cellular phones, wireless local area network enabled computing devices, and radio frequency identification (RFID), or more dangerously, the intentional radio frequency threat sources from terrorists. Thus, it is of interest to determine the path loss from a transmitting device inside the cabin of a transport aircraft to the RF input of a potential victim system of the aircraft. Given this "interference path loss" (IPL) and an estimate of the power radiated by the transmitter, we can determine the power delivered to the victim system and compare this power to known thresholds for vulnerability [2][3] to determine margin of safety.

Understanding of the nature of the path loss from emitters in the passenger cabins to the communication and navigation systems has evolved over the last two decades of data collection through measurements. Previous efforts to measure IPL directly have demonstrated that accurate and repeatible measurements are difficult to obtain, resulting in large variances with sensitive dependence on the measurement techniques employed; examples include [4],

[5], [6], and [7]. An example of IPL analysis demonstrating the deleterious impact of IPL uncertainty is presented in [8].

Past modeling work attempting to explain and quantify this mechanism by comparison of *in situ* measurements to measurements made under controlled conditions using simplified mock-ups have not yielded satisfactory results [9][10]. In those experiments, the comparison showed similarities in path loss between the aircraft mock-up data and actual aircraft data. However, the aircraft path loss was larger [9]. The finding from these studies is that the variation in path loss with distance and radius is unpredictable and remains unexplained.

The limited success of previous efforts combined with the need for this analysis has prompted us to develop a methodology to explain the phenomena which leads to an improved understanding of path loss. The methodology we have developed is based on combining several methods including a technique we refer to as Power Balance Theory (PBT) and the Uniform Geometrical Theory of Diffraction (UTD). Our method predicts the interference path loss through a 3-part process. In the first part, we estimate the power which escapes the cabin through windows. In the second part, we treat radiating windows as magnetic currents on a perfectly conducting cylinder modeling the fuselage exterior, and determine the resulting electric field at the location of the victim antenna. In the third part, we estimate the power delivered to the victim antenna from the incident electric field using a simple model for the antenna. A comparison of simulated and measured values shows that there is a significant correlation between the simulated and measured results, albeit with a small number of outliers. Excluding these outliers, the results seem to agree within about 5 dB.

This thesis is organized as follows. Chapter 2 ("Theory") explains the methods we use in this thesis and how they model the scenario of interest as an electrically conducting cylinder within which a transmitter is emitting power. The chapter also discusses the factors that affect the results. Chapter 3 ("Proposed Method") outlines our solution, which consists of applying the methods discussed in Chapter 2 to the aircraft problem. Chapter 4 ("Results") presents our results, which include a comparison between our simulated results and measured

results for eight different aircraft. The differences between simulated and measured results are discussed. Chapter 5 ("Conclusions") summarizes the results of this thesis and proposes future work that could improve the results presented here.

Chapter 2

Theory

Consider a modern transport aircraft which includes a large cabin. The cabin could be passenger space, cargo space or some combination of the two. An emitter transmits from an unspecified location in the cabin. The radiated signal propagates within the cabin, where it is either absorbed by lossy objects such as seats or people, or escapes through apertures; in particular, windows. Some fraction of the signal power which escapes from windows radiates safely away from the aircraft, whereas some remaining fraction will propagate along the surface of the fuselage and be received by a "victim" antenna located somewhere along the top (zenith-facing) area of the fuselage. We wish to determine the interference path loss (IPL), which is defined as the ratio of power delivered to the terminals of the victim antenna to the power radiated by the emitter.

This chapter consists of six sections and they are organized as follows: in Section 2.1, we provide an overview of the mechanisms involved in the signal propagating from an emitter to a victim antenna. In Section 2.2, we explain Power Balance Theory (PBT) and how this theory can be used to establish the amount of power that escapes through windows relative to total transmit power. In Section 2.3, we show that this power can be modeled in terms of magnetic current moments on a smooth, windowless cylinder. In Section 2.4, we determine the electric field on the surface of a smooth perfectly conducting cylinder due to a

magnetic current moment found in Section 2.3. In Section 2.5, we explain how to calculate the power delivered to the victim antenna due to the electric fields found from Section 2.4. In Section 2.6, we explain how anticipated phase differences in magnetic currents from window to window affect the power delivered to the victim antenna and the IPL.

2.1 Propagation Basics

The power radiated by a transmit antenna is reflected and diffracted by walls, ceilings, floors, or other objects which are conductive or which have high permittivity. This scattering continues until all power is either (1) absorbed by some lossy material or (2) escapes through apertures to the outside. Lossy material includes interior furniture and human bodies.

We are interested in the power that escapes through apertures, propagates along the exterior surface, and reaches the victim antenna. A rigorous solution to this problem involves the solution of an integral equation that is prohibitively numerically intensive when the cavity is large compared to a wavelength. We therefore seek a simpler method. In this method, we choose to first find the ratio of the power that escapes through windows, P_{window}, to the total power, P_T. We then find the ratio of power received at the victim antenna, P_R, to P_{window}. This process can be expressed mathematically as

$$P_T \left(\frac{P_{window}}{P_T} \right) \left(\frac{P_R}{P_{window}} \right) = P_R \ . \tag{2.1}$$

Thus, we can find IPL as:

$$\text{IPL} \cong \frac{P_R}{P_T} = \left(\frac{P_{window}}{P_T} \right) \left(\frac{P_R}{P_{window}} \right) \ . \tag{2.2}$$

The factor $\left(\frac{P_{window}}{P_T} \right)$ is calculated using Power Balance Theory (PBT) and the factor $\left(\frac{P_R}{P_{window}} \right)$ is determined through the Uniform Geometrical Theory of Diffraction (UTD).

2.2 Calculating Power Escape Through Windows Using Power Balance Theory

The problem of radiation from a window in an aircraft cabin can be likened to the problem of radiation from an aperture in a lossy cavity with conducting walls. Hill *et al.* [11] developed a simple method for estimating the disposition of power transmitted by the source in this scenario. We refer to this approach as Power Balance Theory. The advantage of this method is that it does not require details of cavity geometry, the aperture geometry, and the geometry and material characteristics of the objects inside the cavity.

The key quantity in this analysis is Q, quality factor, which is interpreted as the ratio of energy dissipation over a period $1/f$, to the total available power, where f is the transmit frequency. In our problem, the cavity is treated as microwave cavity having an overall quality factor given by:

$$Q = \omega U_s / P_d \tag{2.3}$$

where $\omega = 2\pi f$, U_s is the steady state energy in the cabin in response to the steady state source, and P_d is the power dissipation in the cabin. The dissipated power can be written as the sum of four contributions:

$$P_d = P_{d1} + P_{d2} + P_{d3} + P_{d4} \tag{2.4}$$

where P_{d1} is the power dissipated through losses in the cavity walls, P_{d2} is the power absorbed by objects within the cavity, P_{d3} is the power lost through aperture leakage, and P_{d4} is the power absorbed by receiving antennas inside the cavity. The overall Q can be written as:

$$\frac{1}{Q} = \frac{1}{Q_1} + \frac{1}{Q_2} + \frac{1}{Q_3} + \frac{1}{Q_4} \tag{2.5}$$

where $Q_1 = \omega U_s/P_{d1}$, $Q_2 = \omega U_s/P_{d2}$, $Q_3 = \omega U_s/P_{d3}$, and $Q_4 = \omega U_s/P_{d4}$.

The individual loss mechanisms are explained in the following subsections.

2.2.1 Wall Losses

For metallic walls, Q_1 is given by

$$Q_1 = \frac{3V}{2\mu_r S\delta} \tag{2.6}$$

where $\mu_r = \mu_\omega/\mu_0$, V is cavity volume, S is cavity surface area, δ is the skin depth $\sqrt{2/\omega\mu_\omega\sigma_\omega}$, μ_0 is magnetic permeability of free space, μ_ω is the permeability of the wall material, and σ_ω is the conductivity of the wall material.

2.2.2 Absorption Loss

Q_2 is expressed in terms of the total mean absorption cross section of all lossy objects in the cavity, $\langle\sigma_a\rangle$, as follows:

$$Q_2 = \frac{2\pi V}{\lambda\langle\sigma_a\rangle} \tag{2.7}$$

where λ is the free space wavelength. The mean in this case is over all directions of incidence. We weigh all directions as equally probable, which is assumed to be valid on the basis that we expect copious scattering within the cavity. The total absorption due to M lossy objects, $\langle\sigma_a\rangle$, can be expressed as

$$\langle\sigma_a\rangle = \sum_{i=1}^{M}\langle\sigma_{ai}\rangle \tag{2.8}$$

where $\langle\sigma_{ai}\rangle$ is the mean absorption cross section of the ith object. For the scenario of interest,

i in Equation 2.8 indexes absorption by people, seats, wiring, etc.

2.2.3 Aperture losses

Q_3 is primarily determined by the number of apertures and their sizes. Q_3 is expressed as:

$$Q_3 = \frac{4\pi V}{\lambda \langle \sigma_t \rangle} \tag{2.9}$$

In PBT, only the area – and not the shape – of apertures is important, such that the windows can be modeled as circular apertures of radius a_w. From [11], we find that the mean transmission cross section, $\langle \sigma_{aw} \rangle$, for a single aperture is:

$$\langle \sigma_{aw} \rangle \approx \frac{\pi a_w^2}{2} \quad \texttt{if} \quad ka_w > 1.29 \tag{2.10}$$

i.e., for electrically large apertures; or

$$\langle \sigma_{aw} \rangle \approx \frac{16}{9\pi} k^4 a_w^6 \quad \texttt{if} \quad ka_w < 1.29 \tag{2.11}$$

for electrically small apertures.

We then express the total transmission cross section as

$$\langle \sigma_t \rangle \approx N_w \langle \sigma_{aw} \rangle \tag{2.12}$$

where N_w is the total number of apertures.

2.2.4 Losses due to receiving antennas

Antennas which are part of other devices in the cabin can absorb power. If we assume there are antennas inside the cavity, the worst case condition in terms of maximum power absorption occurs when each antenna is resonant and attached to a matched load. In these conditions, Q_4 is expressed as:

$$Q_4 = \frac{16\pi^2 V}{m\lambda^3} \tag{2.13}$$

where m is the number of antennas.

2.2.5 Summary - Power Escape through Windows

The goal of this analysis is to determine the ratio of power escape through windows (P_{window}) to total transmit power (P_T), for use in Equation 2.2. Since P_T must equal total power dissipated (P_d), we have

$$L_w = \frac{P_{window}}{P_T} = \frac{P_{d3}}{P_d} = \frac{\omega U_s/Q_3}{\omega U_s/Q} = \frac{Q}{Q_3} = \frac{1}{Q_3}\frac{1}{\frac{1}{Q_1}+\frac{1}{Q_2}+\frac{1}{Q_3}+\frac{1}{Q_4}} \tag{2.14}$$

We will show in Chapter 4 that Q_1 and Q_4 tend to be relatively large and are therefore not major contributions to Q, resulting in a simpler expression.

In our method, it will be important to know not just the total power escaping from all windows, but specifically the power escaping from each window. We shall assume that the power escaping from each window is equal, independent of the location of the transmitter within the cabin. Of course this cannot be exactly true, since we would expect intuitively that windows closer to the transmitter convey more power than those further away. However, this effect is strongly mitigated by the reverberant nature of the cabin. It is reasonable to assume that each window makes an equal contribution to the overall power that escapes through windows. This is most easily seen from a ray-optical viewpoint: any ray emerging from the transmitter is likely to be reflected many times before escaping through a window; therefore,

the window through which it escapes is essentially random. Evidence for this assumption is presented in [12], in which it is found that the variation from window to window is less than 5 dB at frequencies above VHF.

2.3 A Simple Model for a Radiating Window Using Equivalent Currents

In the previous section, we found the power which escapes the cavity through each aperture. We now consider the problem of how to determine the power delivered to the victim antenna from the aperture.

We begin with the problem of modeling the radiation of power through an aperture. It is well-known that the problem of scattering by transmission through an aperture in a perfectly conducting screen can be modeled as the radiation of magnetic currents over the same area without an aperture [13]. In this procedure, the magnetic currents are determined by the enforcement of electromagnetic boundary conditions on the surface in the vicinity of the aperture. This is not possible in the present problem because we do not have expressions for the fields over the aperture; instead we have only total power radiated by the aperture. To overcome this problem, we model the magnetic current distribution very simply as a pair of orthogonally-polarized magnetic current moments located at the geometrical center of the aperture and oriented tangentially to the surface, as shown in Figure 2.1. Based on the assumption that the escaping electric field is randomly-polarized as the result of many reflections within the cabin, we make another assumption that each polarization of the associated equivalent magnetic current is responsible for one half of the power.

In order to use the model proposed above it is necessary to determine the magnitude of current moments that give rise to the same amount of power known to be escaping from the given window. This can be determined as follows: Consider a current moment $\mathbf{p}_m = I_m L \hat{\mathbf{l}}$,

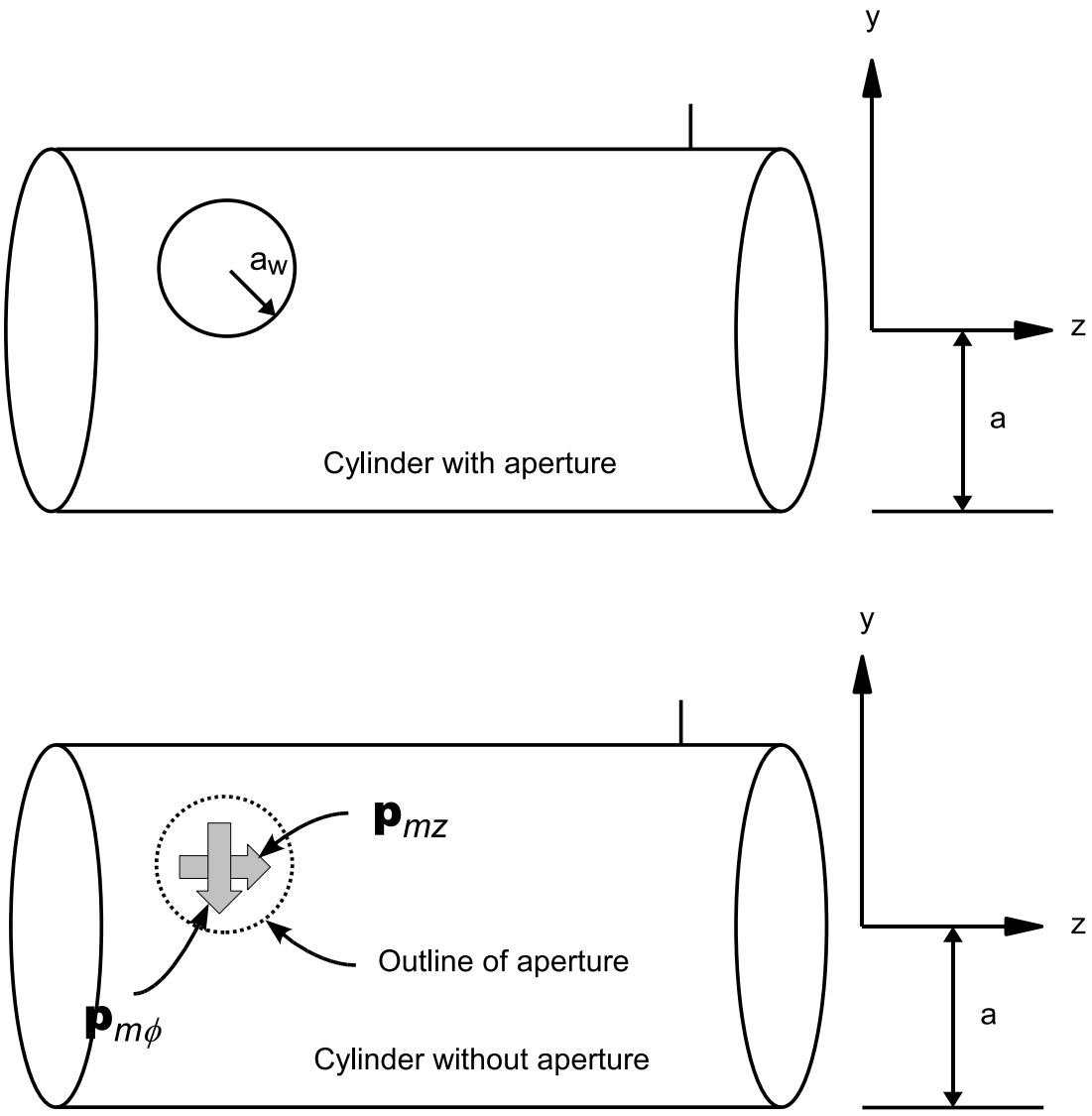

Figure 2.1: Equivalent currents.

where I_m is a complex quantity for magnetic current, and L is length, where it is assumed that $kL << 1$. Here we are concerned primarily with the magnitude of I_m and address the phase later in Section 3.6. $\hat{\mathbf{l}}$ is a unit vector representing the polarization of the current. The far-field electric and magnetic fields arising from this source in free space are

$$\mathbf{E} = -\frac{jkL}{4\pi} I_m \hat{\mathbf{l}} \times \hat{\mathbf{r}} \; \frac{e^{-jkr}}{r} \tag{2.15}$$

and

$$\mathbf{H} = +\frac{jkL}{4\pi\eta} I_m \hat{\mathbf{l}} \times \hat{\mathbf{r}} \times \hat{\mathbf{r}} \; \frac{e^{-jkr}}{r} \tag{2.16}$$

where k is the free space wavenumber $2\pi/\lambda$, and $\hat{\mathbf{r}}r$ is the vector pointing from the source point to the field point.

The power P_p radiated by $\mathbf{p}_m$ in these conditions is determined by computing the Poynting (power density) vector $\mathbf{S}$ associated with field described in 2.15 and 2.16, and then integrating this over a sphere in the far-field to determine the total power passing through the sphere. One finds

$$\begin{aligned} \mathbf{S} &= \frac{1}{2}\mathbf{E} \times \mathbf{H}^* \\ &= \frac{1}{2}\left(\frac{-jkL}{4\pi}\right)\left(\frac{jkL}{4\pi\eta}\right)^* (-\hat{\mathbf{r}}\sin^2\theta)\frac{1}{r^2}|I_m|^2 \\ &= \frac{1}{2\eta}\left(\frac{kL|I_m|}{4\pi r}\right)^2 \hat{\mathbf{r}}\sin^2\theta \end{aligned} \tag{2.17}$$

where θ is the angle between $\hat{\mathbf{l}}$ and $\hat{\mathbf{r}}$; thus, $\hat{\mathbf{l}} \times \hat{\mathbf{r}} = \hat{\boldsymbol{\phi}} \sin\theta$, and $\hat{\mathbf{l}} \times \hat{\mathbf{r}} \times \hat{\mathbf{r}} = \hat{\boldsymbol{\theta}} \sin\theta$.

$$\begin{aligned} P_p &= \oint \mathbf{S} \cdot \hat{\mathbf{r}} ds \\ &= \frac{1}{2\eta} \left(\frac{kL|I_m|}{4\pi r} \right)^2 \int_{\phi=0}^{2\pi} \int_{\theta=0}^{2\pi} \sin^2\theta \hat{\mathbf{r}} \cdot \hat{\mathbf{r}} a^2 \sin\theta d\theta d\phi \\ &= \frac{k^2 L^2 |I_m|^2}{12\pi\eta} \\ &= \frac{k^2 (|\mathbf{p}_m|)^2}{12\pi\eta} \end{aligned} \tag{2.18}$$

where η is the intrinsic impedance of free space ($\approx 377\Omega$).

Since the total power radiated by $\mathbf{p}_m$ in the presence of a perfectly conducting surface must be the same as that in the absence of the conducting surface, and since we wish for each current moment $\mathbf{p}_{m\phi}$ and $\mathbf{p}_{mz}$ to account for half the total power radiated by the window, we have

$$\mathbf{p}_{m\phi} = \hat{\phi} \sqrt{\frac{12\pi\eta P_p}{k^2}} \tag{2.19}$$

and

$$\mathbf{p}_{mz} = \hat{z} \sqrt{\frac{12\pi\eta P_p}{k^2}} \tag{2.20}$$

where $P_p = P_T L_w / (2N_w)$.

2.4 The Electric Field on the Surface of a Smooth PEC Cylinder due to a Magnetic Current Source

In the previous section, we defined magnetic current sources that generate the same amount of power as that which escapes a window. We are now interested in finding the electric field due to these sources incident on a victim antenna on the fuselage exterior. This problem can be solved rigorously using integral equation techniques but this is very computationally intensive when a wavelength is small compared to the scattering structure, in this case, the fuselage. We therefore propose a simpler approximate solution illustrated below.

We first consider the behavior of the electric field radiated by each window individually. The solution to the canonical problem of a magnetic current moment on a perfectly conducting right circular cylinder is provided by Pathak and Wang (1981) [14]. This solution is in terms of the Uniform Geometric Theory of Diffraction (UTD). In this solution, the field propagates as a ray along a geodesic path between the source point (G') and observation point (G) as shown in Figure 2.2. A geodesic path is defined as the shortest path between two points on a surface.

The surface radius of curvature in the plane perpendicular to the z axis, a, is assumed to be electrically large, and the curvature in other planes is smaller or zero. The medium exterior to the convex surface is free space. The surface electric field at G due to a magnetic source at G' on the perfectly conducting cylinder is then given by

$$\begin{aligned}\mathbf{E}_m &= \frac{-jk}{4\pi}\mathbf{p}_m \\ &\quad \cdot \left[2\left(\hat{\mathbf{b}}'\hat{\mathbf{n}}\left\{\left(1-\frac{j}{kt}\right)V(\xi)\right.\right.\right. \\ &\quad \left. + T_0^2\frac{j}{kt}[U(\xi)-V(\xi)]\right\} \\ &\quad \left.\left. + \hat{\mathbf{t}}'\hat{\mathbf{n}}\left\{T_0\frac{j}{kt}[U(\xi)-V(\xi)]\right\}\right)\right]\frac{e^{-jkt}}{t} \end{aligned} \tag{2.21}$$

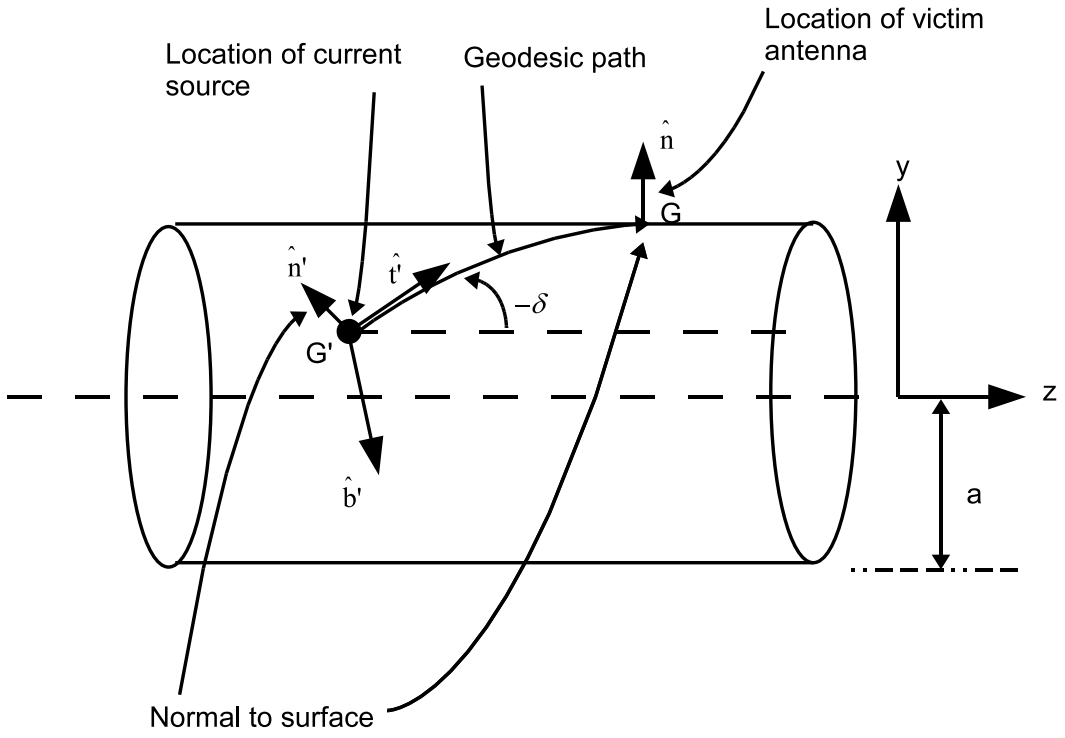

Figure 2.2: The geodesic path that starts at a source point G' and ends at point G on the cylinder.

where

- t is the distance from the source to the field point along the geodesic path. Using the coordinate system implied above, we have for our problem $t = \sqrt{(a\Delta\phi)^2 + \Delta z^2}$ where $\Delta\phi$ is the angular change between source point and field point point along ϕ. Δz is the separation along z.
- $\hat{\mathbf{n}}$ is the unit normal vector at the field point (i.e., at the location of the victim antenna).
- $\hat{\mathbf{t}}'$ is a unit vector tangent to the surface, pointing from the source point in the direction of the geodesic to the field point.
- $\hat{\mathbf{b}}' = \hat{\mathbf{t}}' \times \hat{\mathbf{n}}'$.
- $T_0 = \cot\,\delta$, where δ is the angle, measured in the plane tangent to the source point, between the axis of the cylinder and $\hat{\mathbf{t}}'$.
- $\xi = mt/\rho_g$ where $m = (k\rho_g/2)^{1/3}$, ρ_g is the surface radius of curvature in the ray direction, and $\rho_g = a/\sin^2\,\delta$.
- $V(\xi)$ is the "hard surface" Fock integral. Here, we use the numerical approximation suggested in [15], described in Appendix A.
- $U(\xi)$ is the "soft surface" Fock integral. Here, we use the numerical approximation suggested in [15], described in Appendix A.

Note that Equation 2.21 is written in compact dyadic notation; for example, $\mathbf{p}_m \cdot \hat{\mathbf{b}}'\hat{\mathbf{n}}$ is interpreted as $(\mathbf{p}_m \cdot \hat{\mathbf{b}}')\hat{\mathbf{n}}$. Consequently, we see that the electric field is completely $\hat{\mathbf{n}}$-polarized, as required by the relevant boundary condition $\mathbf{E}_m \times \hat{\mathbf{n}} = 0$.

Given the expression above, we wish to investigate the propagation behavior of the electric fields. Figure 2.3 and 2.4 show how fast the fields decay as they propagate away from the source in different directions. The source has a magnitude of 1 volt-meter (V·m) and is

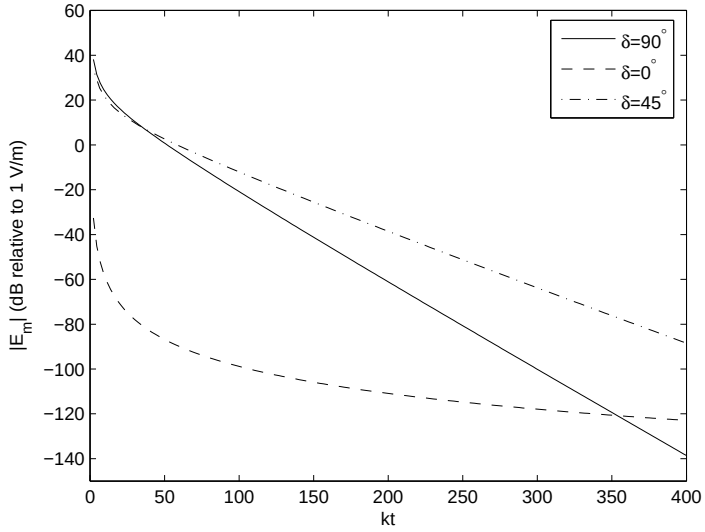

Figure 2.3: Variation of electric fields along different paths, excited by $\hat{z}$-polarized magnetic current source for $ka = 65.9$. $kt = 414.5$ corresponds to the circumference of a cylinder of radius $a = 2$ m.

$\hat{z}$-polarized or $\hat{\phi}$-polarized. Propagation paths examined are along z-axis ($\delta = 0°$), perpendicular to z-axis ($\delta = 90°$) and half way between these two ($\delta = 45°$). The length of the path is measured in terms of kt when $ka = 65.95$. This value of ka corresponds to $a = 2.0$ m at 1575 MHz, the GPS L1 frequency. This frequency is used because we shall use it in subsequent examples.

2.5 Power at the Terminals of an Antenna in Response to Incident Electric Field

The electric field incident on the victim antenna is the sum of the electric fields due to the $2N_w$ individual current moment sources, each calculated separately according to the Equation 2.21. The resulting power P_R delivered to the antenna terminals under matched load conditions [13] is

$$P_R = \frac{1}{8R_A}|\mathbf{E}_t \cdot \mathbf{l}_e|^2 \tag{2.22}$$

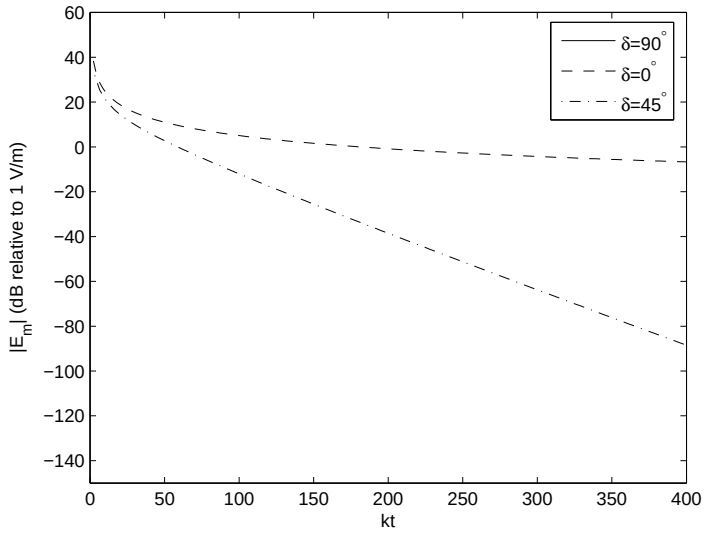

Figure 2.4: Variation of electric fields along different paths, excited by $\hat{\phi}$-polarized magnetic current source for $ka = 65.9$. The $\delta = 90°$ result is below the bottom edge of this plot.

where R_A is the radiation resistance (i.e., the real part of the antenna impedance), $\mathbf{E}_t$ is the sum of all $\mathbf{E}_m$, and $\mathbf{l}_e$ is the vector effective length of the victim antenna. For an ideal thin quarter-wave monopole, $R_A \approx 36\Omega$ and $\mathbf{l}_e = \hat{\mathbf{n}}\lambda/2\pi$. Although this is not necessarily an accurate model for any other antenna that might be used, a quarter-wave monopole serves as useful "worse case" scenario from an IPL perspective since it has maximum gain uniformly distributed along the horizon. The result for any other antenna can be calculated by applying the expected difference in gain in the tangent (horizon) plane with respect to that of a quarter-wave monopole. We will discuss this difference in detail in Chapter 4.

2.6 Randomly Phased Contributions Arriving at Each Window

In the previous section, we have neglected the phase of the current sources. Clearly, the current source phases are not expected to be equal; instead, we expect them to be uniformly

randomly distributed. To account for this phase difference, we assign a randomly-generated phase to each magnetic source when calculating the electric fields. Therefore, some electric field contributions add constructively, and some add destructively. The resulting total field, $\mathbf{E}_t$, is used to calculate the final power delivered to the victim antenna and to calculate the IPL. We employ a "Monte Carlo" technique to determine the distribution of possible IPL values. The minimum IPL is obtained when the electric fields add in phase.

Chapter 3

Proposed Method

We now apply the theory described in Chapter 2 to the aircraft problem. Given a transmit antenna emitting inside the fuselage, we wish to find the power escape through the windows, and the power that eventually reaches the victim antenna, located on top (dorsal region) of the fuselage. To do this, we will first determine the Q associated with the cavity modeling the fuselage, and use this to establish the fraction of power that escapes through windows. Once the power from each window is known, we then determine the equivalent magnetic currents $\mathbf{p}_{m\phi}$ and $\mathbf{p}_{mz}$ that generate the same amount of power at each window. Once the magnetic currents are known, we will find the total electric field excited by these $2N_w$ magnetic sources incident on the victim antenna, using UTD. The sum of the fields determines the power delivered to the antenna, taking into account the random distribution of the phase of the electric field from each source. We also adjust our results to account for the gain of the antenna of interest. This process is illustrated through the flowchart shown in Figure 3.1.

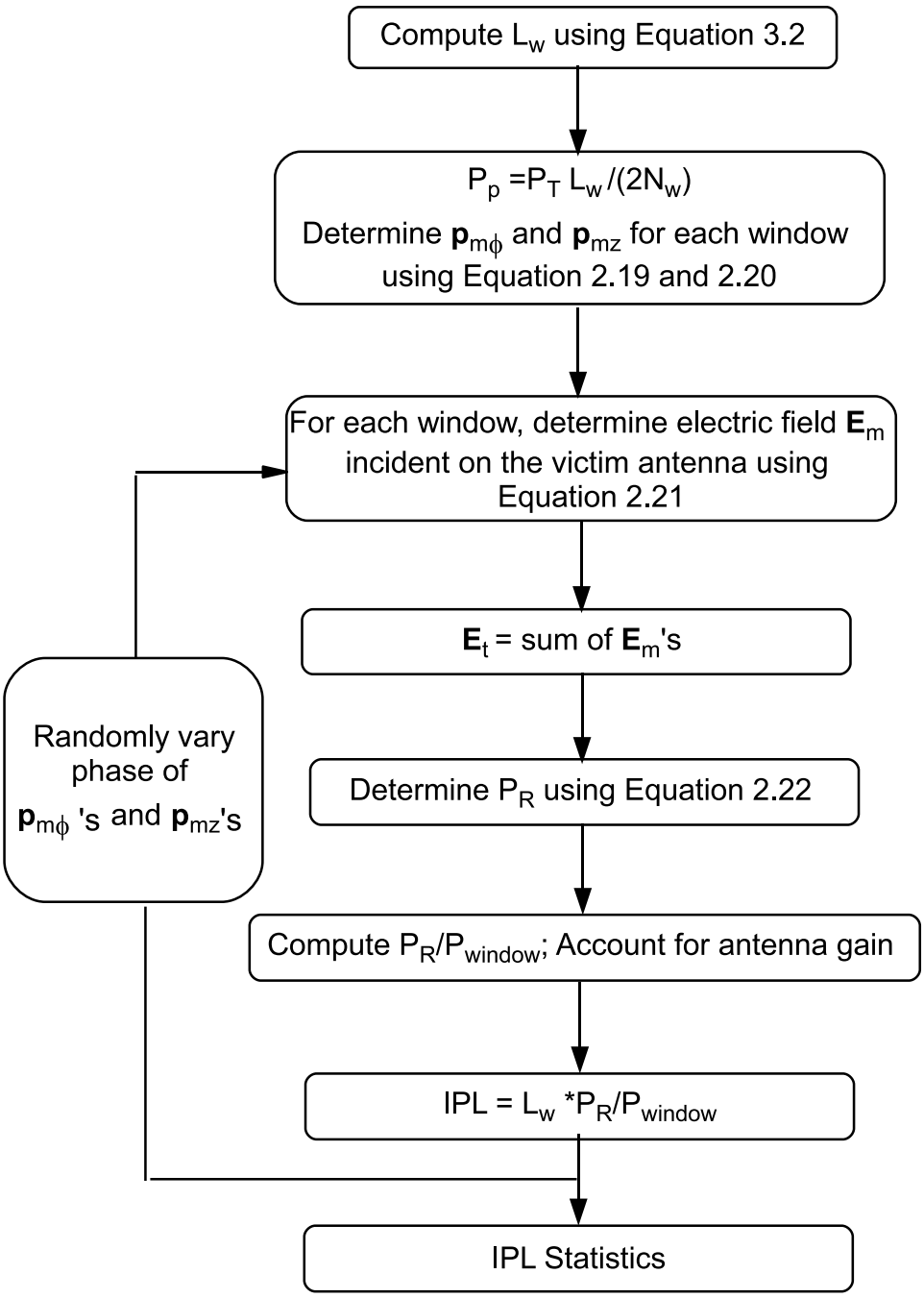

Figure 3.1: Method to determine the IPL statistics from an emitter inside the fuselage to a victim antenna located on exterior surface of the fuselage.

3.1 Parameterized Aircraft Model

To begin our problem, we first model the aircraft fuselage as a cylinder. If we place the cylinder in the Cartesian coordinate system, the z-axis is pointing toward the tail of the fuselage, and the y-axis is pointing out the top (zenith-facing) side of the fuselage, as shown in Figure 3.2. Note this is also where the victim antennas are located. The reason that we choose the antennas located at dorsal area is that there is no need to account for the influence of wings, engines or other structure. We also neglected the possibility that door seams might disrupt the surface propagation along the path between the window and the antenna.

The new parameters introduced in this model, shown in Figure 3.3, are as follows: a_w is the window radius, as we treat the window as a circular aperture; α_w is the angle from x-axis at which the center of the window is located; and θ_g is the offset angle from the y-axis, where the victim antenna is located.

To compute L_w, we require an estimate of the volume of the cabin. We estimate the volume given the length of the fuselage L_f as follows:

$$V = (0.8L_f)(\pi a^2)\frac{1}{2} \tag{3.1}$$

where we have assumed the cabin is 80% of the length of the fuselage, and 1/2 is an estimate of the cabin volume relative to the volume of the equivalent cylinder.

The aircraft considered are listed in Table 3.1, along with the relevant dimensions. In the table, n_{wg} corresponds to the cabin window number, counting on one side from the front towards the back, above which the GPS antenna is approximately located. Regardless of their actual spacing, the windows are assumed for the purposes of our calculations to be evenly spaced along the length of the cabin.

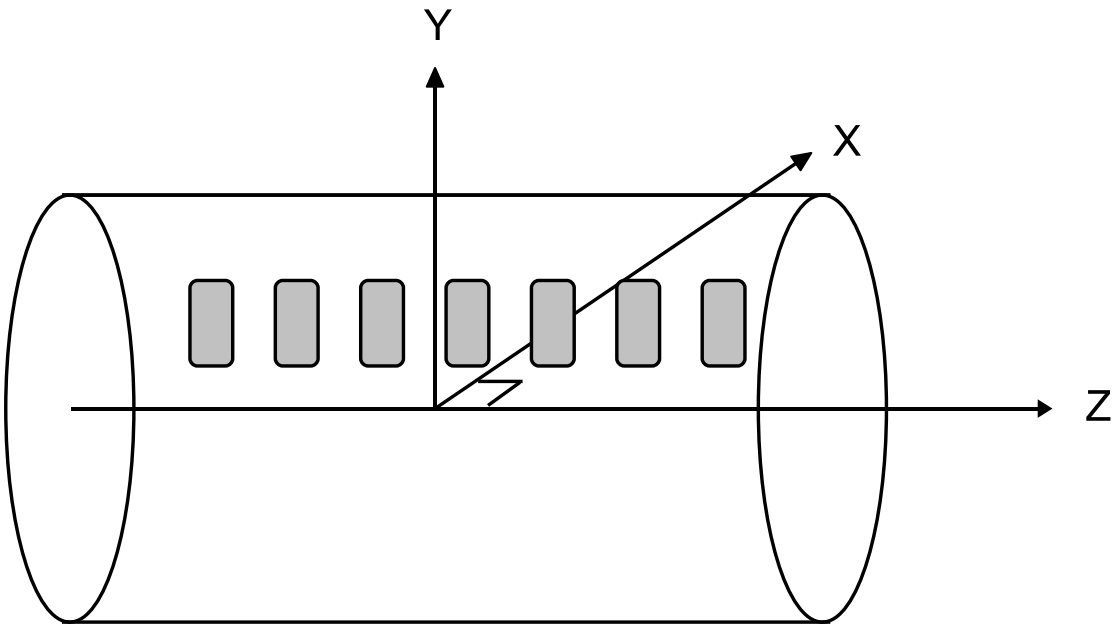

Figure 3.2: The aircraft fuselage is modeled as a cylinder.

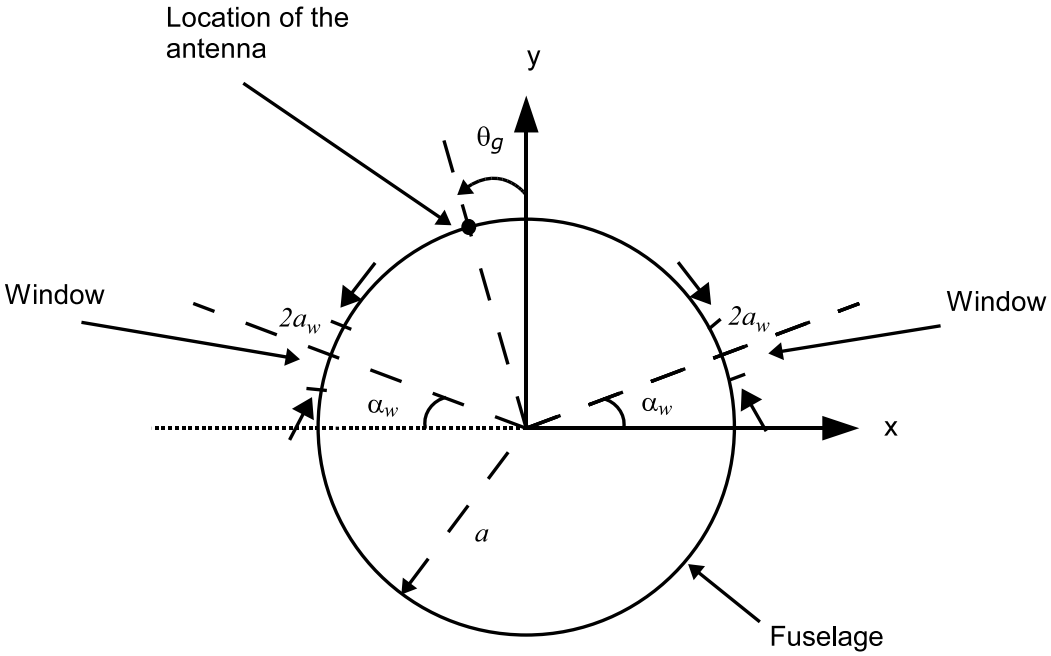

Figure 3.3: The front view of a partial aircraft fuselage.

Aircraft	Cabin Radius a [m]	Fuselage length L_f [m]	Number of Seats N_s	Number of Windows N_w	Window Radius a_w [cm]	Window Pos. α_w	* Ant. n_{wg}	* Ant. θ_g
B727-200	1.88	41.5	134	94	(14)	(20)	(9)	(0°)
B737-200	1.88	29.4	110	66	(14)	(20)	9	5°
B747-400	2.42	68.8	416	194	(14)	(20)	(9)	(0°)
B767-400	2.52	54.9	261	106	(14)	(20)	(9)	(0°)
B777-200	3.11	62.9	305	128	(14)	(20)	(9)	(0°)
A330-300	2.82	63.6	295	132	(14)	(20)	(9)	(0°)

Table 3.1: Aircraft considered in this study. Dimensions indicated in parentheses are estimated from drawings or photos. See text and Figure 3.3 for additional information. * n_{wg} and θ_g provided here are for the GPS antenna, which will be covered as an example later.

3.2 Quality Factors

We now consider the problem of determining the cabin quality factors, Q_1 - Q_4, last discussed in Section 2.2. We shall do this by example, using the Boeing B737-200 aircraft.

3.2.1 Wall loss

Q_1, associated with wall losses, is typically large and varies with wall conductivity, σ_w. Note that by "wall", we are referring to the outer skin of the aircraft, which is typically metallic. For reference, σ_w is 3.78×10^7 S/m for aluminum. Figure 3.4 shows Q_1 as a function of frequency for 3 values of σ_w. As the wall conductivity increases, Q_1 increases. Since Q measures how well the cavity stores energy, high Q_1 indicates the loss due to wall is low. We conclude that Q_1 can be assumed to be greater than 10^5 for aluminum walls at UHF.

3.2.2 Absorption loss

Q_2 is associated with losses due to absorption within the fuselage. To find Q_2, we require reasonable estimates of absorption cross section, $\langle \sigma_{ai} \rangle$. We assume that the sum of lossy

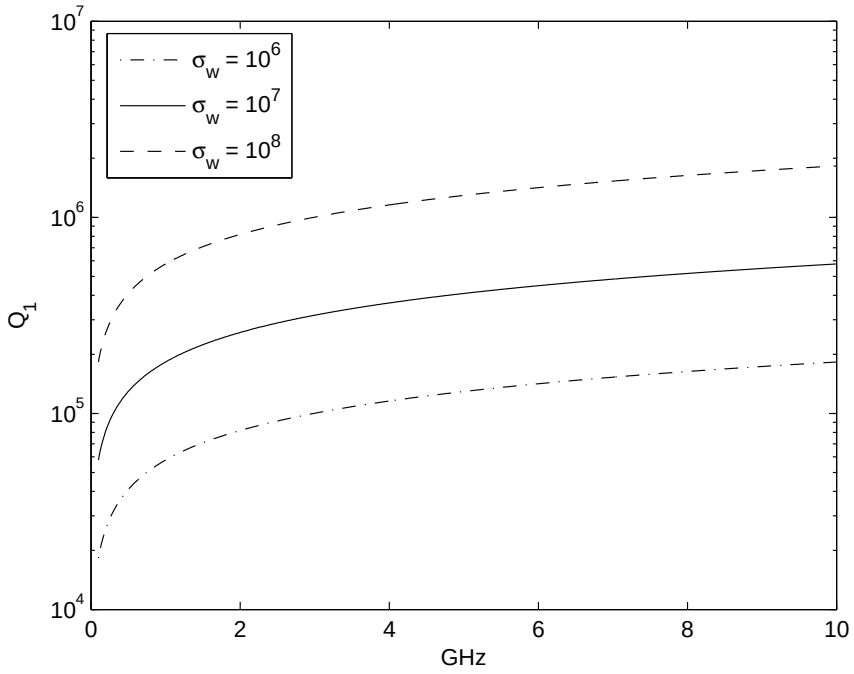

Figure 3.4: Change of Q_1 with respect to different σ_w.

material is accounted for by the combination of people and seats, and that all other material in the cabin has negligible loss in comparison. The mean absorption cross section of a typical person is about 0.4 m^2 at 2.4 GHz, and varies very slowly with frequency [16]. The absorption cross section of a typical seat is known to be approximately 0.04 m^2 at microwave frequencies, again varying very slowly with frequency [17]. Using these values, Figure 3.5 shows the relationship between Q_2 and passenger occupancy, as a function of frequency. The plot shows that higher the passenger loading, the lower Q_2 is at a given frequency. Note that $Q_2 < 10^3$ for frequency less than 4 GHz in all cases.

3.2.3 Aperture loss

To calculate Q_3, which is associated within the loss through apertures, we require reasonable estimates of total mean aperture cross section, $\langle \sigma_t \rangle$. We assume this loss is entirely attributable to windows, as opposed to other apertures such as gaps around doors, or con-

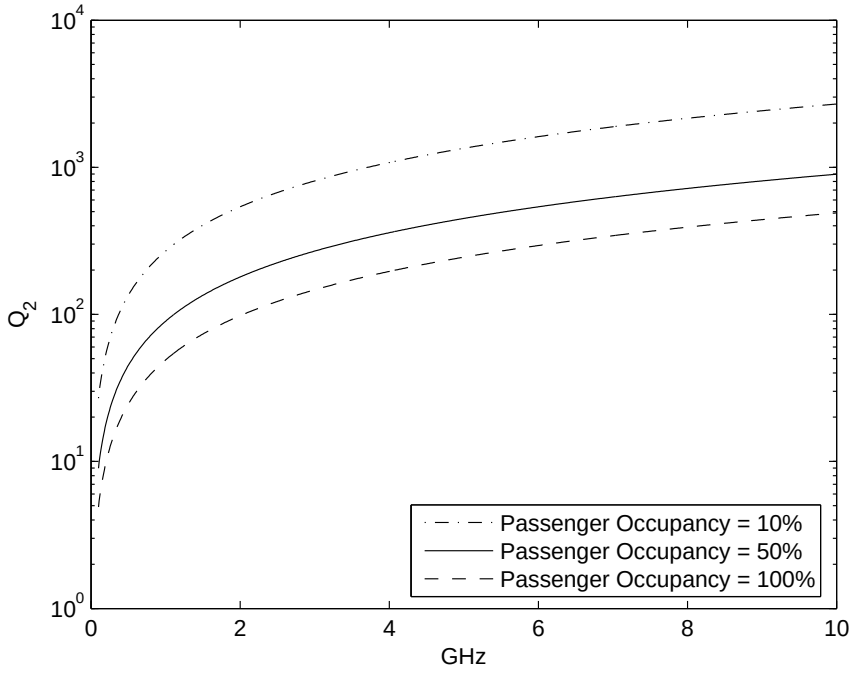

Figure 3.5: Change of Q_2 with respect to passenger loadings at different frequencies.

ducted emission via wires. Evidence indicating that transmission through windows is in fact the dominant mechanism for escape from an aircraft cabin appears in [18]. Figure 3.6 shows the relationship between Q_3 and number of windows, provided the mean cross section of the window is determined using Equation 2.10 or 2.11 with $a_w = 14$ cm. From the plot, we see that more windows lead to a smaller Q_3. Note that $Q_3 < 10^4$ for frequency less than 4 GHz in all cases.

3.2.4 Losses due to antenna

Q_4 deals with dissipation of power via antenna on other devices in the cabin. Recall that our expression for Q_4 assumes matched load conditions. In reality, these antennas will generally not be matched at the frequency of interest. Thus, we are exploring the extreme case scenario by assuming this and further assuming that the B737-200 is fully occupied and every passenger carries a device with a matched load antenna. Figure 3.7 shows the

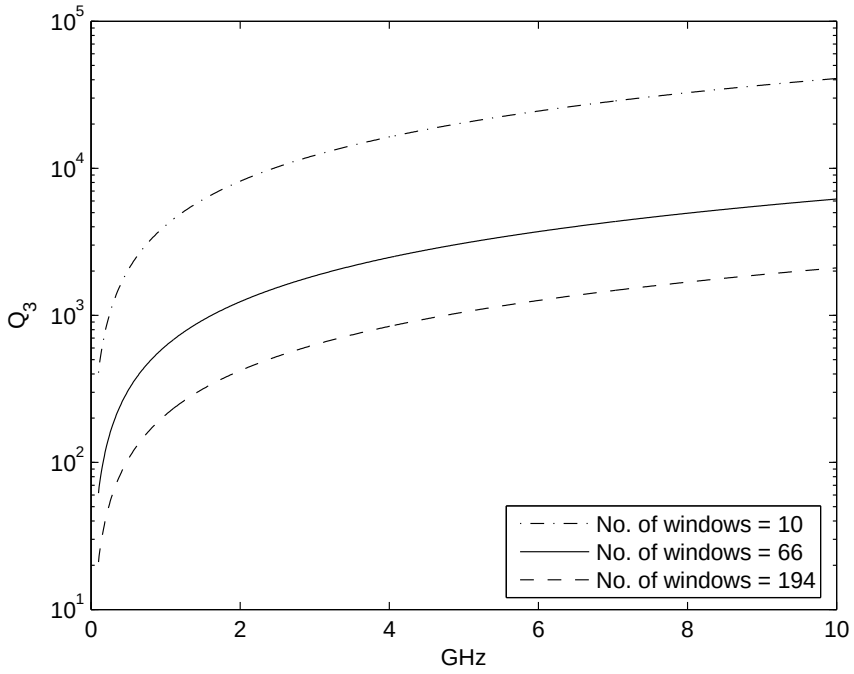

Figure 3.6: Change of Q_3 with respect to number of windows.

relationship between Q_4 and number of antennas in the cabin. When there are more antennas to absorb the power, the loss due to antenna is greater and hence Q_4 becomes lower. Note that $Q_4 > 10^4$ for frequency greater than 1 GHz in all cases.

3.2.5 Summary

We wish to generalize the behavior of the Qs in order to determine how significant each Q is relative to others. Table 3.2 summarizes the Q values for a B737-200 at different frequencies assuming wall conductivity (for aluminum) $\sigma_w = 3.78 \times 10^7$ S/m as in Section 3.2.1. We further assume that the aircraft has 0% passenger load and that there are no matched-load antennas inside the cabin. Under such assumptions, Q_1 and Q_4 are large compared to Q_2 and Q_3, as shown in Table 3.2.

When the above-mentioned assumptions are changed, the Qs are changed as well. First

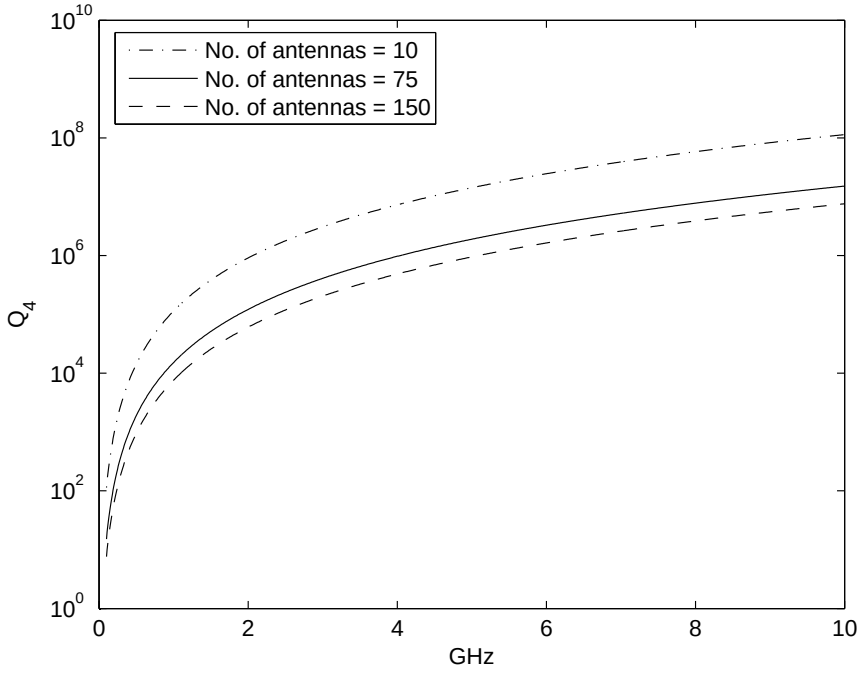

Figure 3.7: Change of Q_4 with respect to number of antennas.

note that as passenger load increases, Q_2 decreases for all frequencies, while Q_1, Q_3 and Q_4 remain the same. This observation makes sense because only Q_2 is associated with losses due to absorbing bodies such as people. Also note that when there are matched-load antennas within the cabin, Q_4 is no longer ∞. As a matter of fact, Q_4 is greatly affected by the number of the antennas inside the cabin. Figure 3.8 demonstrates that above 3 GHz, Q_4 is large compared to Q_2 and Q_3, even for the worst-case scenario (when there is a matched-load antenna per passenger and the aircraft is 100% loaded with passengers). Below 3 GHz but above 1 GHz, Q_4 varies greatly depending on how many matched-load antennas are in the cabin: If less than 10% of the passengers have a matched-load antenna, then Q_4 is still large compared to Q_2 and Q_3; If more than 10% of passengers have a matched-load antenna, then Q_4 is not significantly greater than Q_2 and Q_3. Below 1 GHz, Q_4 is actually quite small regardless the number of antennas inside the cabin. For example, Q_4 is as small as 10 and 250 at 118 MHz and 330 MHz, respectively, for the worst-case scenario; and is 110 and 2.5×10^3 for the scenario when 10% of passengers have a matched-load antenna. In other

	118 MHz	330 MHz	1227 MHz	5060 MHz
Q_1	1143152	191170	368625	748580
Q_2	78	205	765	3155
Q_3	61722	2821	3313	13664
Q_4	∞	∞	∞	∞

Table 3.2: Q_1, Q_2, Q_3, and Q_4 at four key frequencies for a B737-200 with $\sigma_w = 3.78 \times 10^7$ S/m assuming 0% passenger load.

words, Q_4 is not greater than Q_2 and Q_3 no matter how many matched-load antennas are inside the cabin below 1 GHz.

If we consider frequencies above 3 GHz for any number of matched-load antennas in the cabin, Q_1 and Q_4 become insignificant to the overall Q, from Equation 2.5. Therefore, $\frac{1}{Q} \approx \frac{1}{Q_2} + \frac{1}{Q_3}$, and thus the power that escapes through windows is reduced from Equation 2.14 to the following:

$$L_w = \frac{P_{window}}{P_T} = \frac{Q}{Q_3} \cong \frac{(Q_2^{-1} + Q_3^{-1})^{-1}}{Q_3} = \frac{Q_2}{Q_2 + Q_3} \tag{3.2}$$

If we consider frequencies between 1 GHz and 3 GHz, Equation 3.2 is still valid when less than 10% of passengers have a matched-load antenna, but becomes invalid when more than 10% of passengers have a matched-load antennas. For frequencies in the range of 118 MHz and 1 GHz, the use of Equation 3.2 is only strictly valid when when there are no matched-load antennas in the fuselage. When these conditions are violated, the use of Equation 3.2 may cause discrepancies between the calculated IPL and the published measurement.

3.3 Electric Field Radiated by Windows

Finding Qs leads us to find the fraction of power that escapes through the windows. If we assume the power emitted by the antenna in the cabin to be 1 W, we then know the amount

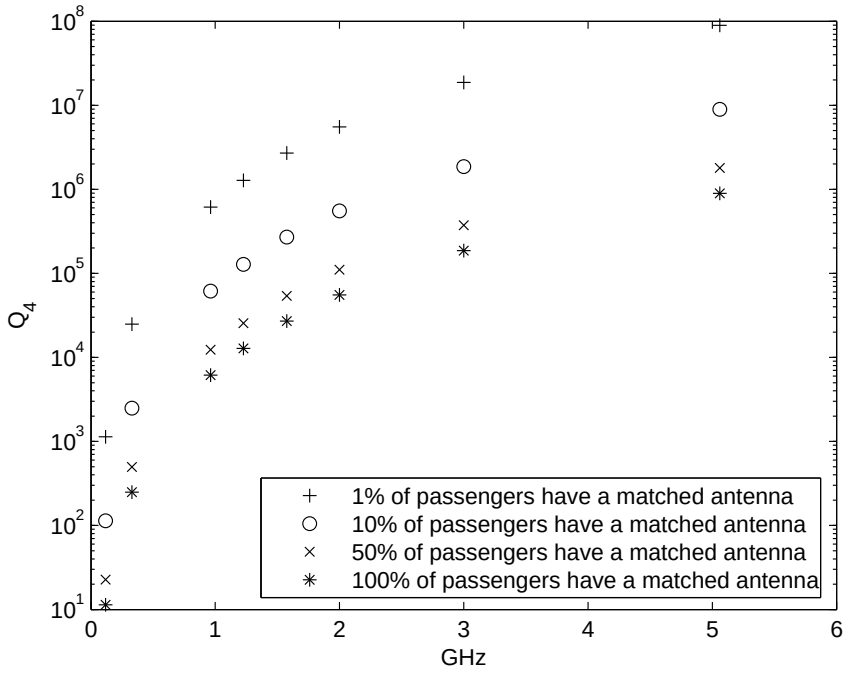

Figure 3.8: Q_4 as a function of frequency and number of matched-load antennas.

of power that goes out through all windows. The power at each window is therefore

$$P_p = P_T L_w/(2N_w) \tag{3.3}$$

Once again we take B737-200 for an example. Assume that the aircraft is 30% full and transmit freqency is 1575 MHz. The power lost through all windows is -12.6 dB, and the power lost through one window is estimated to be 0.83 mW if the transmit power is 1W. Now that we know the power at each window, we can find magnetic currents from Equation 2.19 and 2.20. In this example, the magnitude of each magnetic current moment $\mathbf{p}_m$ turns out to be about 0.10 V-m.

At this point, we are interested to find the change of magnitude of electric field along different paths due to the magnetic current moment with both polarizations, as calculated above. There are 33 windows that are evenly spaced on each side of the aircraft, the aircraft radius $a = 1.88$ m, fuselage length $L_f = 29.5$ m. We will consider the GPS antenna which is

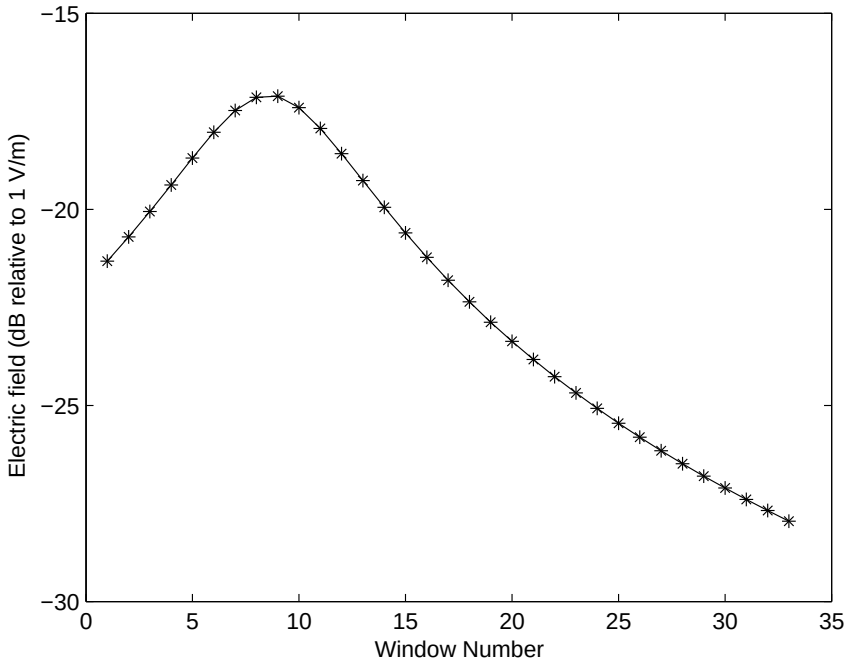

Figure 3.9: The magnitude of electric field from each window individually to the victim antenna, excited by a $\hat{z}$-polarized magnetic current source with magnitude of 0.10 V-m at each window.

located approximately above window 9 counting from the front and has a 5° offset from y-axis. The spacing between windows is assumed to be 57 cm, using effective fuselage length divided by number of windows on one side. The electric fields excited from the $\hat{z}$- and $\hat{\phi}$-polarized magnetic current sources, propagating along the geodesic path on the fuselage from each window to victim antenna, are shown in Figure 3.9 and 3.10, respectively. It is immediately noticed that the polarization effect is pronounced. A maximum in magnitude in one polarization is a minimum in the other polarization. As expected, the field excited from a $\hat{z}$-polarized magnetic current source peaks at the shortest path and decreases gradually with increasing separation between the window and the antenna. The electric field excited from the $\hat{\phi}$-polarized magnetic current source is minimum at shortest path but increases rapidly with increasing distance to the window and then levels off.

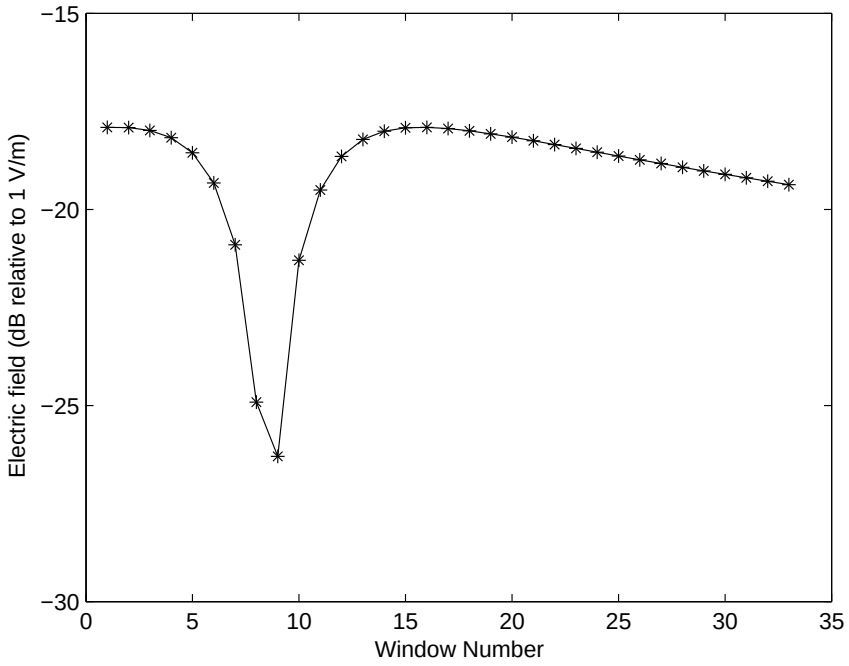

Figure 3.10: The magnitude of electric field from each window individually to the victim antenna, excited by a $\hat{\phi}$-polarized magnetic current source with magnitude of 0.10 V-m at each window.

3.4 Adjustment for Random Distribution of the Phase

At this point, we need to address the issue associated with the expected random nature of the magnetic current phases raised in Section 2.6. Recall we proposed to randomly generate a phase between 0 and 2π and assign this phase to a magnetic source. The sum of the electric fields due to their respective magnetic current source give the total electric field incident on the victim antenna. The total power delivered to the victim antenna, obtained from the total electric field resulting from those source phases, gives one realization of the IPL. From the distribution of trial IPLs, we obtain the mean IPL. The minimum IPL is determined by forcing the electrical fields due to each window to add coherently.

3.5 IPL with Adjustment for Antenna

The proposed method yields the results assuming a quarter-wave monopole, which has a uniform gain of about 5 dBi in all directions along the horizon. Other antennas have different responses. For example, a GPS antenna is typically a patch antenna, which we shall assume to have horizon gain uniformly 19 dB less than that of the reference resonant quarter-wave monopole. This is based on the understanding that the pattern of the patch antenna in the horizontal plane is typically 20 dB below maximum (zenith) gain, which is about 6 dBi [19]. Thus, for GPS, the appropriate correction for results computed assuming a quarter-wave monopole with 5 dBi horizon gain is -19 dB. Appropriate corrections for other antennas/frequencies can be determined similarly.

Chapter 4

Results

In this chapter we present our results under various conditions that would influence the IPL. From Section 3.2, we see that different aircraft configurations or loading factors will lead to different amounts of power escaping through the aircraft windows. Aircraft configurations include the volume of the aircraft, wall conductivity, and number of windows. Loading factors include number of people on board, number of seats and number of absorbing antennas inside the cabin. Section 4.1 presents how the power distribution mechanism changes at different loading factors. Section 4.2 presents IPL results on a window by window basis. Section 4.3 discusses the statistics of IPL distribution. Section 4.4 presents the IPL distribution when the victim antenna is a GPS antenna. Section 4.5 summaries the findings with a specific example.

4.1 PBT Study

In Section 3.2, we observed that the fraction of power that escapes through windows is determined by the cabin Qs, and that the Qs are affected by aircraft configurations and loading factors. We now wish to show how the relative significance of power distribution

mechanisms change with number of people in the cabin, as human bodies are a key factor in terms of power absorption. Even though we mentioned in Section 3.2.5 that power losses due to walls and interior antennas are insignificant, we still include them in this analysis in order to demonstrate they are indeed insignificant. We assume wall conductivity is 3.54×10^7 S/m, and frequency is 1575 MHz, corresponding to GPS L1.

For the 8 aircraft we have studied, Table 4.1 shows where power is dissipated with 100% loading (one passenger per available seat). The loss through windows is 1.4% - 2.4%. Almost 90% of the power is lost through human absoption when the aircraft is fully occupied. When the aircraft is 50% full with passengers, Table 4.2 indicates that about 80% of power is absorbed by people and less than 5% of power escapes through windows. When there are no people on board, a significant amount of the power (13.3 - 45.9%) escapes through windows, as shown in Table 4.3. In all three cases, the losses due to wall and antennas are indeed negligible (0 - 2%).

Aircraft	Seats %	People %	Windows %	Walls %	Antennas %
B727-200	8.9	88.5	2.4	0	0.2
B737-200	8.9	88.8	2.1	0	0.2
B747-400	8.9	89.3	1.6	0	0.2
B767-300	8.9	89.5	1.4	0	0.1
B777-200	8.9	89.4	1.4	0.1	0.1
A330-300	8.9	89.5	1.5	0	0.1

Table 4.1: Power dissipation when the aircraft is fully occupied. Zeros indicate the fraction is less than 0.05%.

As expected, when there are fewer people in the cabin to absorb power, more power escapes through windows. To summarize the findings, we plot power escape through windows at all possible loadings from 0 to 100% for 3 different aircraft. Figure 4.1 shows that the power escape through windows is about -17 dB when the aircraft is full and -7 dB when the aircraft is empty for B737-200. Further to this analysis, we wish to investigate the power loss through windows from an extreme scenario where there are no seats installed in the cabin and no

Aircraft	Seats %	People %	Windows %	Walls %	Antennas %
B727-200	15.9	79.4	4.3	0.1	0.4
B737-200	16.0	79.9	3.7	0	0.3
B747-400	16.1	80.7	2.9	0	0.3
B767-300	16.2	81.0	2.5	0	0.2
B777-200	16.2	80.9	2.6	0.1	0.2
A330-300	16.2	80.8	2.8	0.1	0.3

Table 4.2: Power ratio with 50% passenger loading. Zeros indicate the fraction is less than 0.05%.

Aircraft	Seats %	Windows %	Walls %	Antennas %
B727-200	77.0	20.8	0.2	2.0
B737-200	79.7	18.4	0.2	1.7
B747-400	83.4	15.0	0.2	1.4
B767-300	85.2	13.3	0.3	1.2
B777-200	84.7	13.7	0.3	1.3
A330-300	83.9	14.4	0.3	1.4

Table 4.3: Power ratio with seats unoccupied

people on board to absorb power. Table 4.4 indicates that almost all of the power (about 90%) escapes through windows. This shows that people and seats greatly affect the amount of power that escapes through windows.

Aircraft	Windows %	Walls %	Antennas %
B727-200	90.4	1.1	8.5
B737-200	90.4	1.1	8.5
B747-400	90.4	1.1	8.5
B767-300	89.9	1.7	8.4
B777-200	89.6	2.0	8.4
A330-300	89.8	1.8	8.4

Table 4.4: Power distribution for various aircrafts with no seats or people on board.

So far, we have considered only the GPS L1 frequency, 1575 MHz. It is necessary to investi-

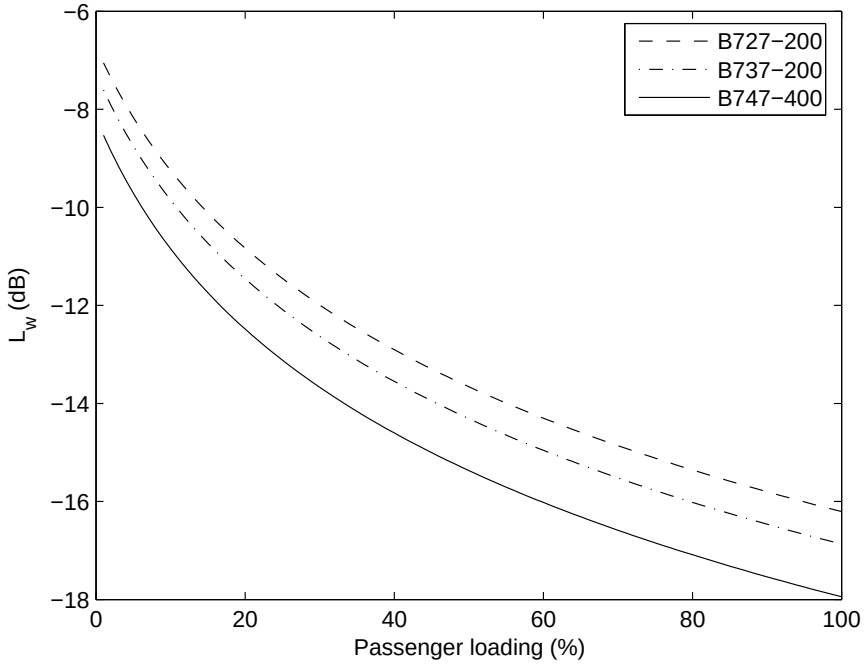

Figure 4.1: Power loss through windows for different aircraft.

gate the variation of power distribution when other frequencies are considered, ranging from VHF to 5 GHz. Specifically, Figure 4.2 shows the fraction of power escape through windows as a function of passenger loading at frequencies of interest: 118 MHz (VOR), 336 MHz (Glide Slope), 1 GHz (DME) and 5 GHz (Microwave Landing System). Based on observations from various simulations, we find that below 500 MHz the fraction of power escaping through windows varies significantly with increasing frequency. However, at frequencies above 500 MHz, the fraction of power escape through windows does not change significantly with increasing frequencies, as shown in Figure 4.2 where the 1 GHz curve overlaps 5 GHz curve.

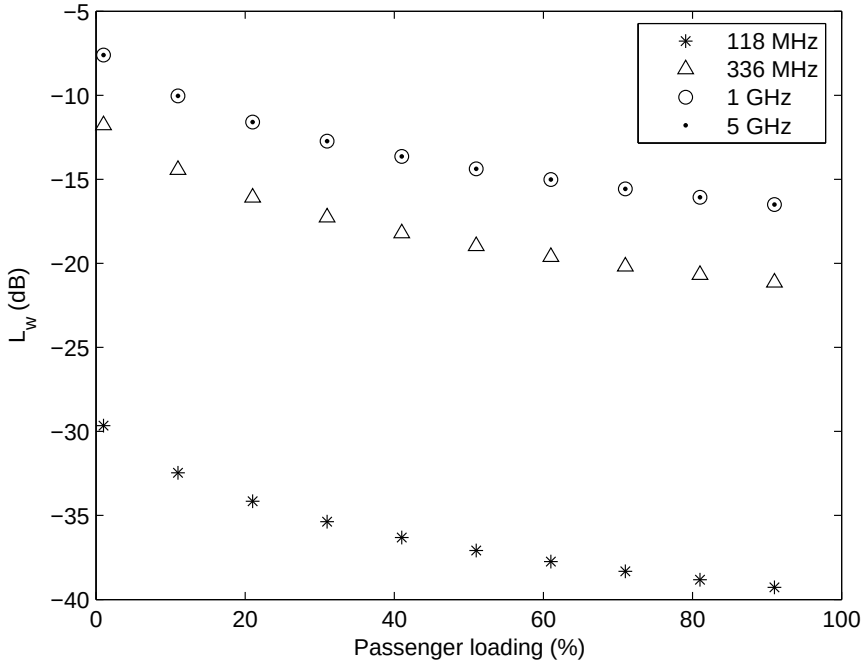

Figure 4.2: Fraction of power escape through windows at different frequencies.

4.2 IPLs on a Window-by-Window Basis

We now wish to consider IPL predicted by our technique for the special case assuming all power escapes from one window. There are two reasons why we choose to do this: 1) Measured results are available for this case, so we can compare our simulated results to the measurements in order to validate the part of our simulation that predicts the power from a window to a victim antenna; and 2) we can gain some insight into the proposed mechanism that will not be available for the total/"all windows" results. The measurements were carried out by M. Jafri, *et al.* [6]. IPLs were measured from each window of a B737 aircraft to the GPS antenna. Measurements were made with a transmitting antenna in vertical ($\hat{\phi}$) and horizontal ($\hat{z}$) polarization at each window.

In our simulation model, each window is assumed to radiate the same amount of power as that emitted by the magnetic current. When antenna is polarized in $\hat{\phi}$, it is equivalent of the

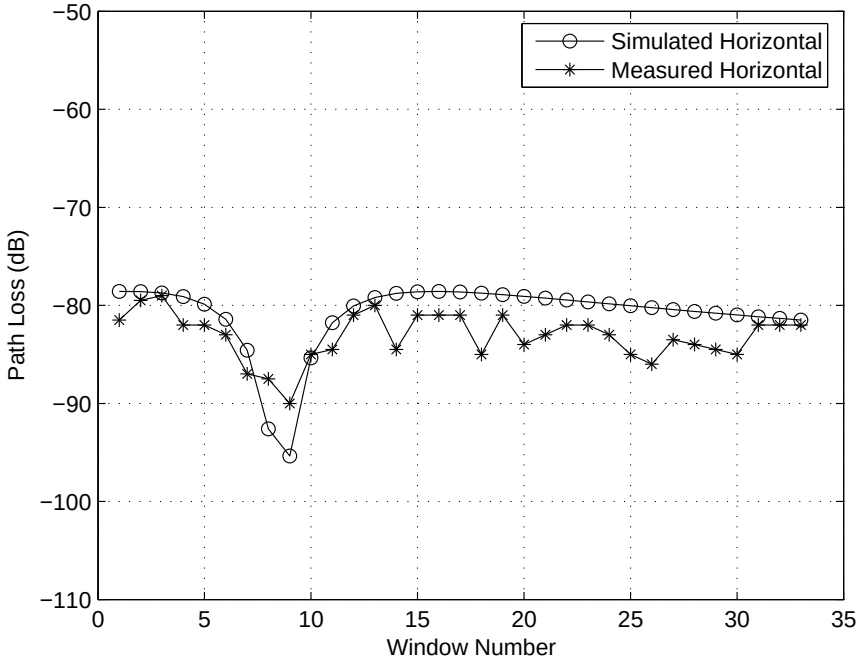

Figure 4.3: Comparison of IPL results for a horizontally-polarized source.

magnetic current moment polarized in $\hat{z}$. When antenna is polarized in $\hat{z}$, it is equivalent of the magnetic current moment polarized in $\hat{\phi}$. We calculate the IPL from each window to the victim antenna, and repeat this process twice for the two polarizations for all 33 windows. This simulation is computed based on a quarter-wave monopole antenna. We assume that the gain of the GPS antenna is uniformly 19 dB less than that of the reference resonant quarter-wave monopole, per Section 3.5.

The calculated IPLs for both polarizations are plotted on Figure 4.3 and 4.4, along with the measured IPL results. The simulated results and measurements indicate that the dominant contributions come from windows close to the GPS antenna (which is above Window No. 9) in the vertical polarization, whereas the dominant contributions come from windows further away from the GPS antenna in the horizontal polarization. The agreement for horizontal polarization is excellent, and the results for vertical polarization also exhibit the expected form but with IPL 5-8 dB less than measurements for the region around Window No. 9.

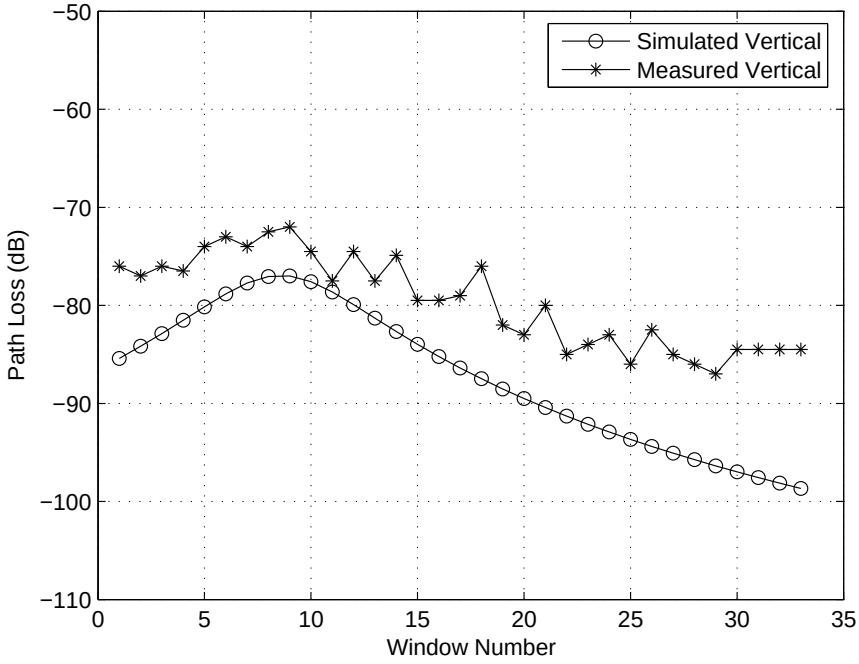

Figure 4.4: Comparison of IPL results for a vertically-polarized source.

4.3 IPL Distribution Statistics

As discussed in Section 2.4, the phase of the magnetic currents is randomly generated between 0 and 2π, and therefore the value of one phase is independent from the value of next phase generated. The resulting fields due to the magnetic currents may add constructively or destructively. Thus, the total field from all the window contributions will be different from one trial to the next. As a result, the IPL will vary from one trial to the next as well. Note the distribution of IPL is similar to Rayleigh in form. Figure 4.5 shows the distribution of IPLs. These IPLs are calculated based on assuming 1575 MHz, a B737-200, there are no passengers on board, and that a quarter-wave dipole is used to model victim antenna located at dorsal region of the fuselage.

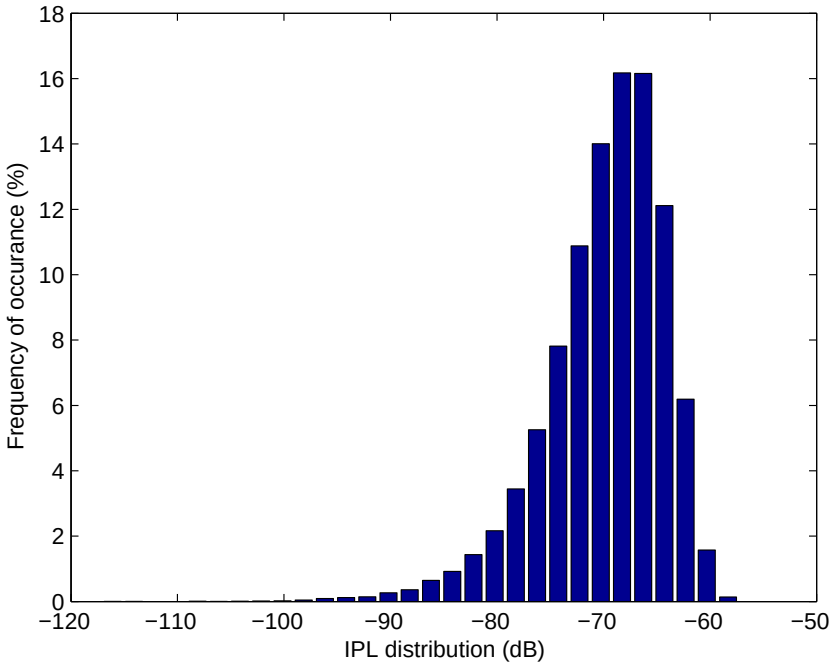

Figure 4.5: IPL distribution after 50,000 trials.

4.4 IPL to a GPS Antenna for Various Aircraft

We now wish to determine IPL for a source well inside the cabin to the GPS antenna located at dorsal area of the aircraft. Results are summarized in Table 4.5. Note we have computed both "minimum IPL" and "mean IPL". The minimum IPL is determined by choosing component electric field phases added coherently to produce the maximum possible field incident on the antenna. The mean IPL is simply the mean of the computed distribution. In some cases, we were able to locate measurements of IPL from various sources as indicated in the rightmost column of Table 4.5.

Figure 4.6 is provided for ease in comparison. We show the comparison for two cases; in one case assuming in the simulation that the aircraft is free of people during the stated measurements, and in the second case assuming 50% passenger load for the simulation. The actual situation in reported measurements is typically not clear. For example, it appears that

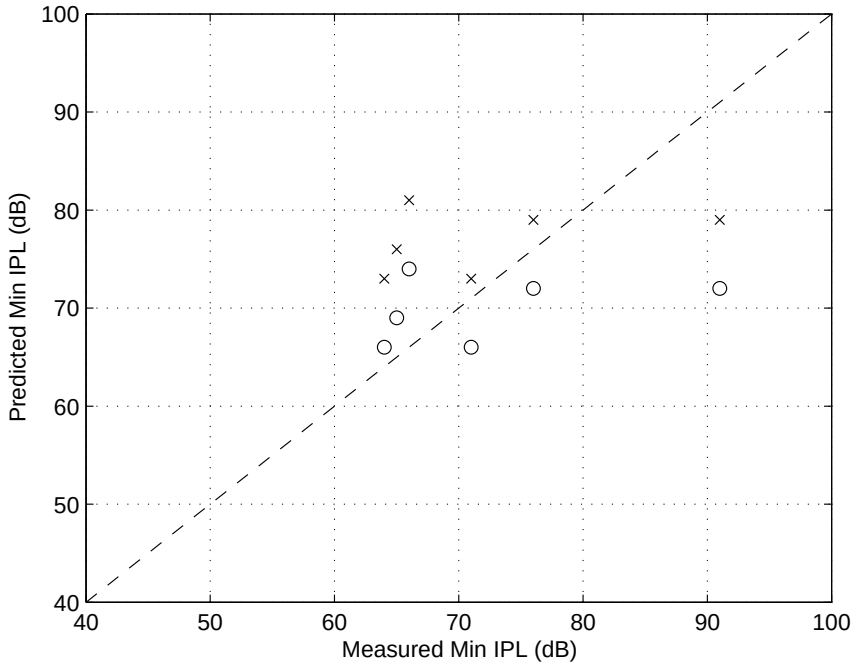

Figure 4.6: Comparison of simulated and measured maximum IPL data from Table 4.5. Circles ("o") correspond to simulations assuming 0% passenger load, whereas the "×" correspond to simulations assuming 50% passenger load. The dashed line corresponds to perfect agreement.

Aircraft	Passenger Load	Simulation Min. [dB]	Simulation Mean [dB]	Measurement Min. [dB]	Ref.
B727-200	Empty	66	87	71	[20, 8]
	50%	73	94		
	Full	75	96		
B737-200	Empty	66	86	64	[21]
	50%	73	93		
	Full	76	96		
B747-400	Empty	69	93	65	[21]
	50%	76	101		
	Full	79	103		
B767-300	Empty	72	93	91	[22]
	50%	79	101		
	Full	81	103		
B777-200	Empty	74	96	66	[22]
	50%	81	103		
	Full	84	106		
A330-300	Empty	72	95	76	[23]
	50%	79	102		
	Full	82	105		

Table 4.5: Results of simulation compared to results of various measurement campaigns. Where no number is indicated, information was not available.

some of the measurements may have involved significant number of workers in the cabin, or may have involved open doors or other conditions which would influence the results. This may account for the large variance in the measured results compared to the relatively small variance observed in the simulated results. Because of the difficulty and possibility for inconsistency in test procedures, it is difficult to know in each case whether it is measurement or simulation that is closer to "true".

Two observations from the simulations are as follows: (1) Regardless of the aircraft considered, the effect of increasing passenger load from 0% to 50% and then 50% to 100% is an increase of about 7 dB and 3 dB in IPL, respectively. (2) The variation from aircraft to aircraft is within an order of magnitude.

f (MHz)	λ (m)	ka	ka_w	0% passenger load L_w(dB)	IPL(dB)	100% passenger load L_w(dB)	IPL(dB)	System
118	2.54	4.6	0.3	-63.4	71	-73.8	81	VOR/VHF
330	0.91	13.0	1.0	-45.5	65	-55.4	75	Glide Slope
962	0.31	37.9	2.8	-7.3	40	-16.9	50	DME
1227	0.24	48.3	3.6	-7.3	44	-16.9	53	GPS L2
1575	0.19	62.0	4.6	-7.3	47	-16.9	57	GPS L1
5060	0.06	199.2	14.8	-7.3	66	-16.9	76	MLS

Table 4.6: Predicted minimum IPL for a dorsal-mounted resonant quarter-wave monopole on a B737 aircraft.

The comparison of simulated and measured values shows that there is a significant correlation between the simulated and measured results, albeit with a small number of outliers. Excluding these outliers, the results seem to agree within about 5 dB.

4.5 IPL Variation with Frequency

We now wish to consider the frequency dependence of IPL for our representative aircraft, the B737-200. Table 4.6 summarizes results for some of the systems that are potentially vulnerable. For the uniform comparison purposes, the antenna is assumed to be a quarter-wave monopole which is resonant at the frequency under study, and located at the same position as the GPS antenna. Note that ka, the electrical radius of the fuselage, is large at all frequencies considered, as required for UTD to be valid. ka_w, the electrical radius of the window, is small at 118 MHz and 330 MHz, which has the effect of choking off power transmission through windows, as can be seen in the results for L_w. This choking-off effect leads to a greater IPL, as indicated for both 0% and 100% loading conditions. As noted in Section 4.1, L_w becomes frequency-independent when windows become electrically large (per Equation 2.10). At higher frequencies, IPL increases due to greater loss in the creeping wave propagation from window to victim antenna. Finally, note that there is a 10 dB IPL difference between 0% and 100% passenger load.

Chapter 5

Conclusions

In this thesis, we have presented a methodology for predicting, through electromagnetic simulation, the IPL for a broad class of aircraft interior-to-exterior propagation problems. The technique yields estimates with minimal computational burden and does not require detailed information about cabin configuration. We demonstrated that the UTD-based method employed by our technique predicts the results of published measurements of window-to-antenna coupling mechanism with reasonable accuracy, using the example of a GPS L1 system on a Boeing 737. We also demonstrated that the complete technique yields statistics for the cabin-to-window IPL which are consistent with published measurements for a number of large transport aircraft.

The data provided by the technique in the investigation reveals that all large transport aircraft exhibit very similar results, and that it is instead the passenger load that is the dominant factor in determining the power transfer coefficient from transmitter to exterior via windows, L_w. It is also found that the difference between 0% and 100% passenger load is about 10 dB in IPL, independent of frequency. The variation in simulation results from aircraft to aircraft is within an order of magnitude for the aircraft considered in this study.

The discrepancies between our results and published measurements may be caused by the

fact that the conditions under which the measurements were taken could be significantly different from our assumed conditions. For example, the number of workers on board during testing is unclear, which affects the resulting IPL measurement. We also assumed that there are no matched-load antennas on board to absorb power for frequencies ranging from 118 MHz to 1 GHz in order to meet the condition of Equation 3.2. It is noted that for the same aircraft model, there are variations in terms of physical interior structure or configuration. For example, the B737-200 has two seating configurations: economy only, and business and economy combined, which affects the number of absorbing objects and their sizes. We modeled the fuselage as a perfect cylinder on which the calculation of volume and surface area was based. In addition, we treat all antennas to be located at the dorsal region of the fuselage to avoid the influence from wings, engines and other structures. Finally, we did not account for the possible interruption along the propagation path; thus interruptions in the fuselage surface such as those due to door seams may change the results.

Further development and improvement is warranted to more clearly determine the fidelity with which our method can predict IPL. Such an effort requires supporting measurements at a variety of frequencies in order to facilitate truly "apples to apples" comparison. It is also desired to obtain specific diagnostic measurements needed to test hypotheses about relevant scattering mechanisms, e.g., testing IPL on a window-by-window basis, doors open vs. doors closed, cabin full vs. cabin empty, and so on. It is also worth noting that the technique described here can be straightforwardly extended to allow calculations for antennas located *anywhere* on the aircraft (not just along the dorsal area), using additional UTD diffraction mechanisms to account for the influence of wings, engines, and other structure. The success of analyzing IPL for antennas located elsewhere on the aircraft will further validate our methodology, and our model may become a simple and useful tool to analyze EMI for any avionic systems on any aircraft. Our effort to obtain an improved understanding of IPL may lead to further research into vulnerabilities of communication and navigation systems and to explore mitigation techniques against future threats.

Appendix A

Fock Functions

The Fock functions $U(\xi)$ and $V(\xi)$ used in Equation 2.21 in Section 2.4 are defined as follows:

$$U(\xi) = \frac{\xi^{3/2} e^{\frac{j3\pi}{4}}}{\sqrt{\pi}} \int_{\infty - j2\pi/3}^{\infty} d\tau \frac{W_2^{'}(\tau)}{W_2(\tau)} e^{-j\xi\tau} \tag{A.1}$$

$$V(\xi) = \frac{\xi^{1/2} e^{\frac{j\pi}{4}}}{\sqrt{2\pi}} \int_{\infty - j2\pi/3}^{\infty} d\tau \frac{W_2^{'}(\tau)}{W_2(\tau)} e^{-j\xi\tau} \tag{A.2}$$

The function $W_2(\tau)$ in above two functions is the Fock-type Airy function defined by:

$$W_2(\tau) = \frac{1}{\sqrt{\pi}} \int_{\infty - j2\pi/3}^{\infty} dZ e^{\tau Z - Z^3/3} \tag{A.3}$$

$W_2^{'}(\tau)$ denotes its derivative with respect to τ .

A numerical method to compute the Fock functions is provided by Burnside, Marhefka and Wang [15]. For $\xi > 0.6$, one employs a rapidly converging series representation for the Fock functions:

$$V(\xi) = e^{-j\pi/4}\sqrt{\pi}\xi^{1/2}\sum_{n=1}^{10}(\tau_n')^{-1}e^{-j\xi\tau_n'} \tag{A.4}$$

$$U(\xi) = e^{j\pi/4}2\sqrt{\pi}\xi^{3/2}\sum_{n=1}^{10}e^{-j\xi\tau_n} \tag{A.5}$$

where τ_n and τ_n' are zeros of $W_2(\tau)$ and $W_2'(\tau)$, respectively, and tabulated in Table A.1.

Table A.1: Tabulated values of $|\tau_n|$ and $|\tau_n'|$

n	$\lvert\tau_n\rvert$	$\lvert\tau_n'\rvert$
1	2.33811	1.01879
2	4.08795	3.24819
3	5.52056	4.82010
4	6.78661	6.16331
5	7.94413	7.37218
6	9.02265	8.48849
7	10.0402	9.53545
8	11.0085	10.5277
9	11.9300	11.4751
10	12.8288	12.3848

For $\xi < 0.6$, one employs a small argument asymptotic expansion for the Fock functions as follows:

$$V(\xi) \approx 1 - \frac{\sqrt{\pi}}{4}e^{j\pi/4}\xi^{3/2} + \frac{7j}{60}\xi^3 + \frac{7\sqrt{\pi}}{512}e^{-j\pi/4}\xi^{9/2} \tag{A.6}$$

$$U(\xi) \approx 1 - \frac{\sqrt{\pi}}{2}e^{j\pi/4}\xi^{3/2} + \frac{5j}{12}\xi^3 + \frac{5\sqrt{\pi}}{64}e^{-j\pi/4}\xi^{9/2} \tag{A.7}$$

The numerical results generated from the equations are plotted in Figure A.1 (magnitude) and A.2 (phase).

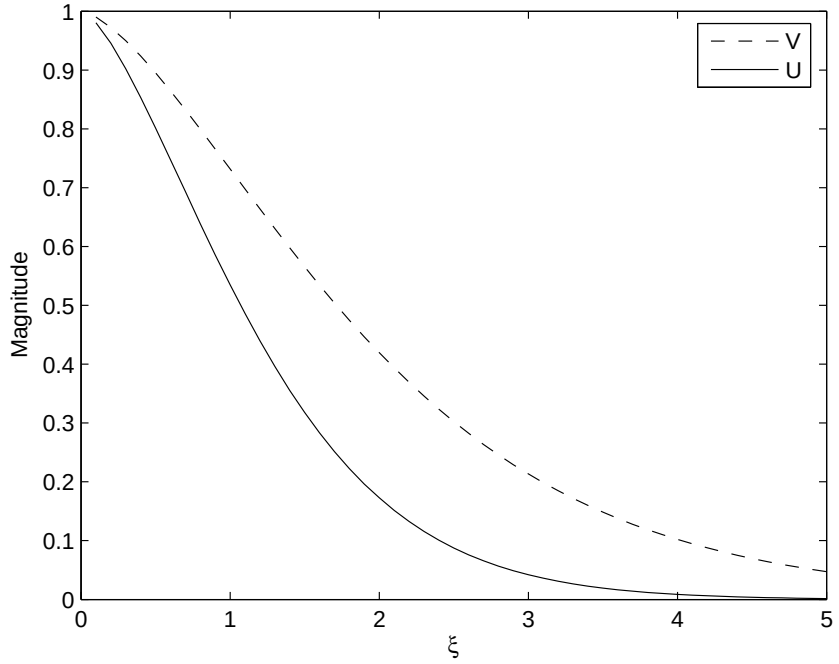

Figure A.1: Fock functions $V(\xi)$ and $U(\xi)$, magnitude.

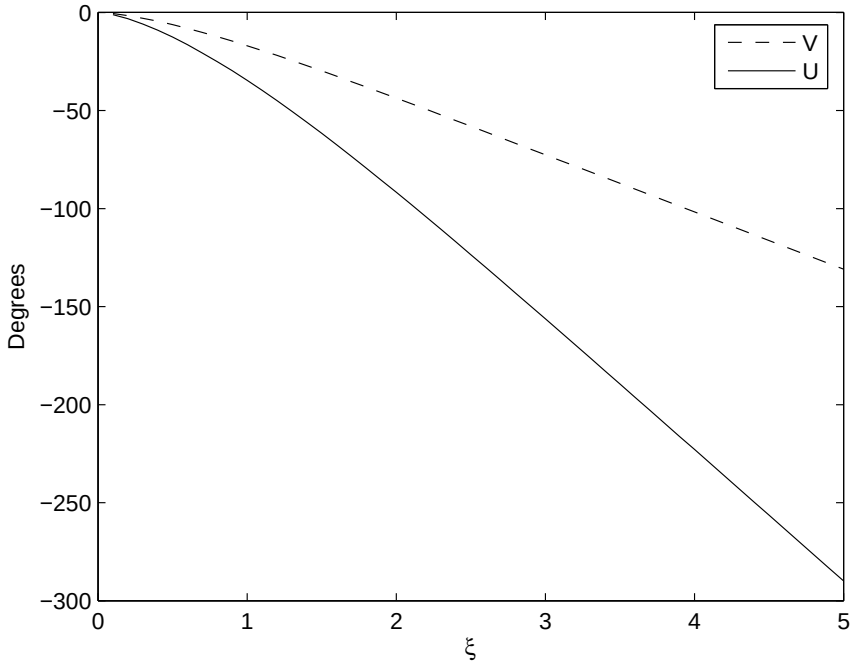

Figure A.2: Fock functions $V(\xi)$ and $U(\xi)$, phase.

Bibliography

[1] U.S. Departments of Defense and Transportation, *2001 Federal Radionavigation Systems*, DOT-VNTSC-RSPA-0103.1/DOD-4650.5, 2001.

[2] RTCA SC-135, "Environmental Conditions and Test Procedures for Airborne Equipment," DO-160E, December 2004.

[3] RTCA SC-202, "Guidance on Allowing Portable Electronic Devices (T-PEDs) on Aircraft." DO-294A, March 2006.

[4] S. Potsch *et al.*, "Reliable Transfer Function Measurements of PED Excitations in Aircrafts," *Proc. IEEE Int'l Symp. Electromagnetic Compatibility*, Vol. 2, August 2003, pp. 537-42.

[5] M. J. Jafri, J.J. Ely, L. Vahala, "Graphical Analysis of B-737 Airplane Pathloss Data for GPS and Evaluation of Coupling Mitigation Techniques," *Proc. IEEE Int'l Symp. Electromagnetic Compatibility*, Vol. 3, August 2003, pp. 832-7.

[6] M. Jafri, J. Ely, L. Vahala, "Comparative Analysis of Interference Path Loss Coupling Patterns on B-737 VS B-757 Airplanes," *Proc. Digital Avionics Systems Conference*, 2005. Volume 1, pp. 6.B.5-1–10.

[7] K. Horton, M. Huffman, B. Eppic, and H. White, "757 Path Loss Measurements," NASA Technical Report CR-2005-213762, June 2005.

[8] J. J. Ely, T. X. Nguyen, S. V. Koppen, M. T. Salud, "Electromagnetic Interference Assessment of CDMA and GSM Wireless Phones to Aircraft Navigation Radios," *Proc. 21st Digital Avionics Sys. Conf.*, Irvine, CA, 27-31 Oct 2002, pp. 13.E.5-1 - 13.

[9] G. Fuller, "Comparison of Cylindrical Mock-up Path Loss Data to Operational Aircraft Data. Determining Path Loss Variations with Distance and Radius at VHF, L Band, and GPS/Satcom," *Proc. 19th Digital Avionics Sys. Conf.*, Philadelphia, PA, 7 -13 Oct 2000, pp. 3.B.4-1 - 8.

[10] G. Fuller,"Path Loss Measurements on Cylindrical Sections: Determining Path Loss Variations with Distance and Radius at VHF, L Band, and GPS/Satcom," *Proc. 19th Digital Avionics Sys. Conf.*, Philadelphia, PA, Vol. 1, 7 -13 Oct 2000, pp. 3.B.3-1 - 8.

[11] D. A. Hill, M. T. Ma, A. R. Ondrejka, B. F. Riddle, M. L. Crawford, and R. T. Johnk, "Aperture Excitation of Electrically Large, Lossy Cavities", *IEEE Transactions on Electromagnetic Compatibility*, Vol 36, No. 3, August 1994, pp. 169-178.

[12] R. W. Devereux, B. Archambeault, G.L Fuller, "Assessment of Analytical Codes for Use in Modeling Aircraft Onboard EMI Threats," *Proc. 16th Digital Avionics Sys. Conf.*, 26-30 Oct 1997, pp. D46/1-D46/8.

[13] W. A. Stutzman and G. A. Thiele, *Antenna Theory and Design*, 2nd Ed., John Wiley and Sons, 1998.

[14] P. Pathak and N. Wang, "Ray Analysis of Mutual Coupling Between Antennas on a Convex Surface", *IEEE Transactions on Antennas and Propagation*, Vol AP-29, No. 6, November 1981, pp. 911-922.

[15] W. D. Burnside, R. J. Marhefka and N. Wang, "Computer Programs, Subroutines, and Functions for the Short Course on the Modern Geometrical Theory of Diffraction." *Appendices for the Short Course on Applications of the Modern Geometrical Theory of Diffraction*, ElectroScience Laboratory, The Ohio State University, Columbus, Ohio, 1984, pp. AP-35 - 37.

[16] S. W. Ellingson, Virginia Polytechnic Institute and State University, personal communication. Unpublished results from previous study, 2003.

[17] T. X. Ngyuen, "RF Loading Effects of Aircraft Seats in Electromagnetic Reverberating Environment", NASA-TM-2000-210626, December 2000.

[18] R. W. Devereux, G. L. Fuller, R. Schillinger, "Further Analysis of the CV-580 and B-727 Aircraft RF Coupling Experiment Data," *Proc. 16th Digital Avionics Sys. Conf.*, 26-30 Oct 1997, pp. 4.1-1-8.

[19] C. A. Balanis, *Antenna Theory: Analysis and Design*, 3rd Ed., John Wiley and Sons, 2005.

[20] RTCA SC-156, "Potential Interference to Aircraft Electronic Equipment from Devices Carried Aboard," DO-199, Sept 16, 1988.

[21] RTCA SC-202, "Guidance on Allowing Transmitting Portable Electronic Devices (T-PEDs) on Aircraft," DO-294A, March 2006.

[22] Delta Airlines, "Delta/NASA Cooperative Agreement NCC-1-381 Deliverable Reports," Delta Engineering Report 10-76052-20, Dec 7, 2000.

[23] EUROCAE Working Group 58, "Report on Electromagnetic Compatibility Between Passenger Carried Electromagnetic Devices and Aircraft Systems," Document ED-118, November 2003. Information obtained via [21].